



# Probing magnetic configuration-mediated topological phases via high harmonic generation in $\text{MnBi}_2\text{Te}_4$

Lei Jia , Zhiya Zhang, D. Z. Yang, and M. S. Si <sup>\*</sup>

*Key Laboratory for Magnetism and Magnetic Materials of the Ministry of Education, Lanzhou University, Lanzhou 730000, China*

G. P. Zhang<sup>†</sup>

*Department of Physics, Indiana State University, Terre Haute, Indiana 47809, USA*



(Received 10 September 2020; revised 5 November 2020; accepted 6 November 2020; published 23 November 2020)

Compared to a space group, a magnetic space group is much more complex, as both magnetic structure and magnetic moment direction can change the original symmetries of materials. The interplay between space symmetry and magnetism can generate versatile novel quantum states. However, detecting these topological phases experimentally, achieved through manipulating the magnetic configuration, has been restricted. It is mainly because the intrinsic link between the theory and the available experimental technique remains elusive. Here, we show that high harmonic generation (HHG) can identify these topological quantum states. We use rhombohedral  $\text{MnBi}_2\text{Te}_4$  film as an example, and analyze the symmetry-dependent harmonic order and signal by combining first-principles calculations and time-dependent Liouville equation numerical computations. Our results provide a fundamental basis for using HHG to study the topological quantum phases mediated by various magnetic configurations that can be easily realized by applying an external magnetic field.

DOI: [10.1103/PhysRevB.102.174314](https://doi.org/10.1103/PhysRevB.102.174314)

## I. INTRODUCTION

One great success in modern condensed matter physics is the introduction of topology absolutely extending the band theory [1,2]. Extraordinary quasiparticles originally predicted in high-energy physics have been realized in the electronic structure of material. The emerged quantum states are established on the notion of topological orders, which are usually correlated with space symmetries. For example, four-fold degenerate bands contacting at discrete momentum points in nonmagnetic materials lead to Dirac semimetals, where the protection of inversion symmetry  $\mathcal{I}$  is necessary [3]. By contrast, according to the Landau's theory, the phases of matter can be understood in terms of spontaneous symmetry breaking. For instance, the breaking of time-reversal symmetry  $\mathcal{T}$  would result in magnetic order. More recently, the interplay of magnetism and symmetry has attracted extensive research attention. It provides a potential platform to study the quantum anomalous Hall effect (QAHE) [4,5], axion electrodynamics [6], and Majorana fermions [7]. Intriguingly, when a material has an antiferromagnetic (AFM) order, both  $\mathcal{T}$  and  $\mathcal{I}$  are usually broken, but their combination  $\mathcal{IT}$  can be respected. This leads the energy band to doubly degenerate at each momentum point. If an additional crystalline symmetry emerges, new quantum phases would arise from an accidental band crossing [8]. However, a method to detect these quantum phases experimentally is still missing.

As a nonlinear response of optics, HHG touches the heart of condensed matter such as symmetries, quantum geometrical nature of electrons, and electron correlation [9–14]. In particular, actively impelling HHG to access a solid enables the construction of an energy band from the normal insulator and/or semiconductor to metal, where HHGs are sensitive to crystalline symmetries [15–18]. In ferromagnets, the breaking of  $\mathcal{T}$  imposes an anisotropic HHG, where the reducing symmetries under spin-orbit coupling (SOC) play a role [18]. In addition, HHG can also probe the topological order from the contribution of edge states, or the sensitive emitted intensities, related to the topological phase boundary [19–21]. Following this guideline, our previous work demonstrated that even harmonics appear in a magnetically doped topological insulator, originating from the breaking of  $\mathcal{I}$  under magnetic doping [22]. However, the results of HHG on breaking both  $\mathcal{I}$  and  $\mathcal{T}$  but keeping the combination  $\mathcal{IT}$  has remained obscure until now. It is thus natural to ask whether HHG can detect the topological quantum states under the interplay between symmetry and magnetism.

In this work, we discover that rhombohedral  $\text{MnBi}_2\text{Te}_4$  film can host four topological phases, which are realized through changing the magnetic configurations. The four topological phases produce four distinct high-harmonic spectra, owing to the interplay between space symmetry and magnetism. For our AFM models, both even and odd harmonics coexist, being protected by  $\mathcal{IT}$ . If there exists crystalline symmetry  $\sigma_{xz}$ , an accidental band crossing will emerge, leading to a Dirac semimetallic state. In addition, only the parallel polarization of harmonics with respect to the laser field is observed. If  $\sigma_{xz}$  is broken through changing the magnetic moment direction, the Dirac point will be gapped, giving

<sup>\*</sup>sims@lzu.edu.cn

<sup>†</sup>Corresponding author: guo-ping.zhang@outlook.com

rise to an axion insulator state. Meanwhile, an additional perpendicular component of harmonics is thus induced. For our ferromagnetic (FM) models,  $\mathcal{IT}$  is broken, whereas  $\mathcal{I}$  is kept. Only odd harmonics are yielded. When the crystalline symmetries  $\sigma_{xz}$  and  $R_y$  hold, a pair of Weyl points appear along the high-symmetry lines  $M'-\Gamma-M$ , generating a Weyl half-semimetallic state. Besides, only the parallel component of harmonics appears. When  $\sigma_{xz}$  and  $R_y$  are broken when rotating the magnetic moment direction, the Weyl points are gapped, leading to QAHE. The perpendicular component of harmonics then arises. In addition, in the FM cases, the nonzero net magnetic moments give rise to the spin HHG, where only even harmonics are allowed. Our results indicate that HHG can identify the topological quantum states induced by different magnetic configurations, which can serve as a benchmark for the corresponding experiments.

The paper is organized as follows. In Sec. II we describe the computational methods that connect the first-principles calculations and HHG. In Sec. III we discuss the distinct HHGs under four topological phases of Dirac semimetal, axion insulator, Weyl half-semimetal, and AHEQ in  $\text{MnBi}_2\text{Te}_4$ . Section IV contains a brief summary and conclusions.

## II. COMPUTATIONAL METHODS

To fully appreciate the nonlinearity of HHG, we use the density matrix method [23,24] to bypass the perturbation theory that is indeed not competent under a strong laser field [25–29]. To accurately obtain the electronic structure of a material, we perform first-principles calculations and solve the Kohn-Sham equation in the framework of density functional theory [23,30],

$$\left[ -\frac{\hbar^2}{2m_e} \nabla^2 + V_{ne}(\vec{r}) + \frac{e^2}{4\pi\epsilon_0} \int \frac{n(\vec{r}')}{|\vec{r} - \vec{r}'|} d^3\vec{r}' + V_{xc}(\vec{r}) \right] \Psi_{n\vec{k}}(\vec{r}) = \epsilon_n \Psi_{n\vec{k}}(\vec{r}), \quad (1)$$

where  $V_{ne}(\vec{r})$  is the potential of the nuclei,  $V_{xc}(\vec{r})$  the exchange-correlation potential, and  $n(\vec{r})$  the electron density.  $\Psi_{n\vec{k}}(\vec{r})$  is the Bloch wavefunction of band  $n$  at crystal momentum  $\vec{k}$ , and  $\epsilon_n$  is the band energy. Before calculating HHG, we self-consistently solve Eq. (1), which is implemented in Wien2k [31]. Once the calculation is converged, we construct the density matrix of the ground state as  $\rho_0 = |\Psi_{n\vec{k}}\rangle\langle\Psi_{n\vec{k}}|$ . Our dynamic density matrix is obtained by numerically solving the time-dependent Liouville equation  $i\hbar\langle n\vec{k}|\partial\rho/\partial t|m\vec{k}\rangle = \langle n\vec{k}[\mathcal{H}, \rho]m\vec{k}\rangle$  [30]. Here, we employ a generic Hamiltonian which reads

$$\mathcal{H} = \mathcal{H}_0 + \mathcal{H}_I(t), \quad (2)$$

where  $\mathcal{H}_0$  is the ground state Hamiltonian that accounts for the electronic energy of a solid and  $\mathcal{H}_I(t)$  is the interaction Hamiltonian between the system and the femtosecond laser pulse. Finally, HHG is computed by Fourier transforming the induced macroscopic polarization  $\vec{P}(t) = \sum_k \text{Tr}[\rho_k(t)\hat{P}_k]$ , with  $\hat{P}_k = -i\hbar\nabla$  being a momentum operator. The nonlinearity of HHG is correlated to the energy dispersion through the dynamic density matrix, which is obtained at the first-principles level.

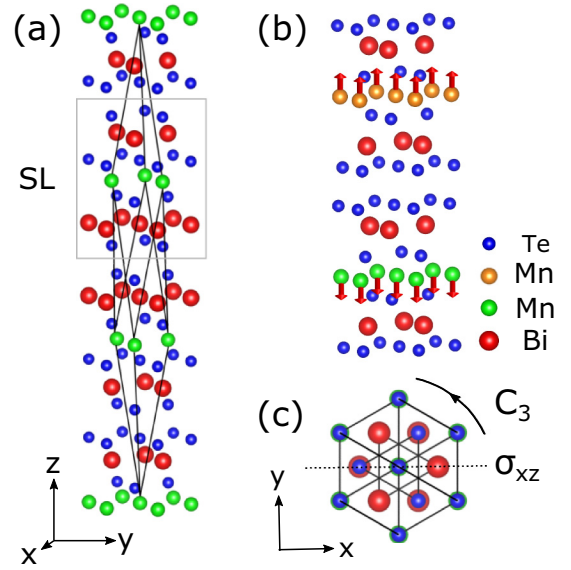


FIG. 1. (a) Crystal structure of the trigonal  $\text{MnBi}_2\text{Te}_4$  with green, blue, and red spheres showing Mn, Te, and Bi atoms, respectively. The nonmagnetic rhombohedral primitive unit cell is indicated by black lines. The gray rectangle denotes the septuple layer (SL). (b) Magnetic structure of 2-SL  $\text{MnBi}_2\text{Te}_4$  corresponding to the interlayer AFM configuration. The arrows on atoms denote the local magnetic moments. (c) Illustration of the mirror and three-fold rotation symmetries  $\sigma_{xz}$  and  $C_3$ , which play crucial role in HHG.

## III. RESULTS AND DISCUSSION

Bulk  $\text{MnBi}_2\text{Te}_4$  is a van der Waals material crystallized in a rhombohedral structure with the space group  $P\bar{3}m2$  [32], consisting of seven-atom layers (e.g., Te1-Bi1-Te2-Mn-Te3-Bi2-Te4) arranged along the trigonal ( $z$ ) axis, known as septuple layers (SLs) [see Fig. 1(a)]. The ground state has an intralayer FM order and an interlayer AFM order, as schematically shown in Fig. 1(b). Since various topological quantum states usually appear in a few SLs of  $\text{MnBi}_2\text{Te}_4$  [33–43], we take 6-SL  $\text{MnBi}_2\text{Te}_4$  as a model to achieve the topological phases under different magnetic configurations. In the nonmagnetic state, 6-SL  $\text{MnBi}_2\text{Te}_4$  has twelve symmetry operations that can be generated by the following three symmetries: the inversion symmetry  $\mathcal{I}$ , the three-fold rotation symmetry  $C_3$ , and the mirror symmetry  $\sigma_{xz}$  [see Fig. 1(c)] [37,39], where  $C_3$  and  $\sigma_{xz}$  are particularly important in our case.

$\text{MnBi}_2\text{Te}_4$  has been experimentally confirmed as an antiferromagnet below the Néel temperature around 25 K [41,44,45], where nonzero magnetic moments on Mn atoms with  $3d$  electrons order antiferromagnetically. The magnetic structure breaks the original crystalline symmetry. In the most energy-favoured AFM structure, the magnetic moments on the space inversion-related Mn atoms are aligned along opposite directions. Therefore, both  $\mathcal{T}$  and  $\mathcal{I}$  are broken, whereas  $\mathcal{IT}$  still holds. Under the consideration of SOC, residual symmetries critically depend on the orientation of magnetic moments.  $\sigma_{xz}$  remains when magnetic moments are along the  $y$  axis [see Fig. 2(a)]. If magnetic moments are along the  $x$  axis,  $\sigma_{xz}$  is broken [see Fig. 2(b)]. With the above two

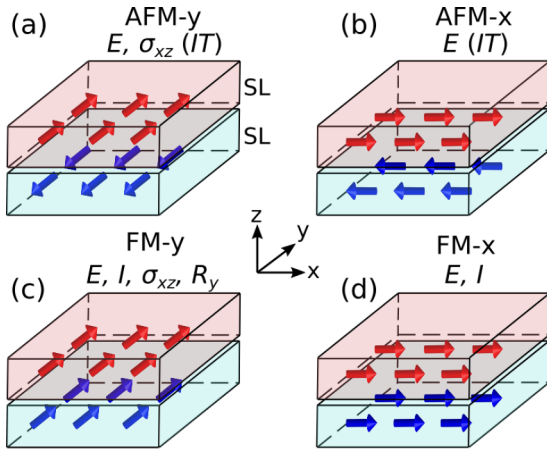


FIG. 2. (a) and (b) Two AFM states holding  $\mathcal{IT}$ . The magnetic moments are along the  $y$  axis, where  $\sigma_{xz}$  holds. However,  $\sigma_{xz}$  is broken, which arises from the magnetic moments along the  $x$  axis. (c) and (d) Two FM states losing  $\mathcal{IT}$ . The magnetic moments along the  $y$  axis restores  $\mathcal{I}$ ,  $\sigma_{xz}$ , and  $R_y$ . Only  $\mathcal{I}$  holds with the magnetic moments along the  $x$  axis.

magnetic configurations, we can study the interplay between  $\sigma_{xz}$  and magnetism in the appearance of  $\mathcal{IT}$ . Certainly, if we want to explore the importance of  $\mathcal{IT}$ , we can design another two FM configurations, where  $\mathcal{I}$  is restored while  $\mathcal{IT}$  breaks, as shown in Figs. 2(c) and 2(d). It is noticed that reflection symmetry  $R_y$  appears when magnetic moments are along the  $y$  axis

The antiunitary  $\mathcal{IT}$  symmetry satisfies  $(\mathcal{IT})^2 = -1$  and guarantees every band doubly degenerates, which is absent in  $\text{Bi}_2\text{Se}_3$  and  $\text{MoS}_2$  [22,46]. If there exists an additional crystalline symmetry, the Dirac point will arise from an accidental band crossing. This is true for the AFM- $y$  configuration, as shown in Fig. 3(a). The Dirac point is located at the crystal momentum  $(-0.015, 0, 0)\pi/a$ , with  $a$  being the in-plane lattice constant, coinciding with the symmetry analysis, see Supplemental Material [31] for more detail. The Fermi energy level exactly intersects the band crossing point, and thus the low-energy excitation can be described by the Dirac equation, making  $\text{MnBi}_2\text{Te}_4$  a promising material for quantum device application. More importantly, such a Dirac semimetallic state is protected by  $\sigma_{xz}$ . Thus, it can survive at the surface. Upon changing the magnetic configuration to AFM- $x$ ,  $\sigma_{xz}$  is broken, gapping the Dirac point, as shown in Fig. 3(b). We find a global band gap of around 40 meV. The intrinsically surface states on the top and bottom sides have half-quantized Hall conductances with opposite signs, indicating an axion insulator state with Chern number  $C = 0$ . This will lead to the topological magnetoelectric effect and the unique magneto-optical Faraday and Kerr effects [39,47,48].

To experimentally detect the above topological quantum states is actually not an easy task as few experimental techniques are available such as angle-resolved photoemission spectroscopy, quantum oscillation experiments, anisotropic negative longitudinal magnetoresistance, anomalous Hall effect, and low-temperature photoelectron spectroscopy [49–54]. Here, we propose HHG as a potential method to distinguish these novel quantum states under sym-

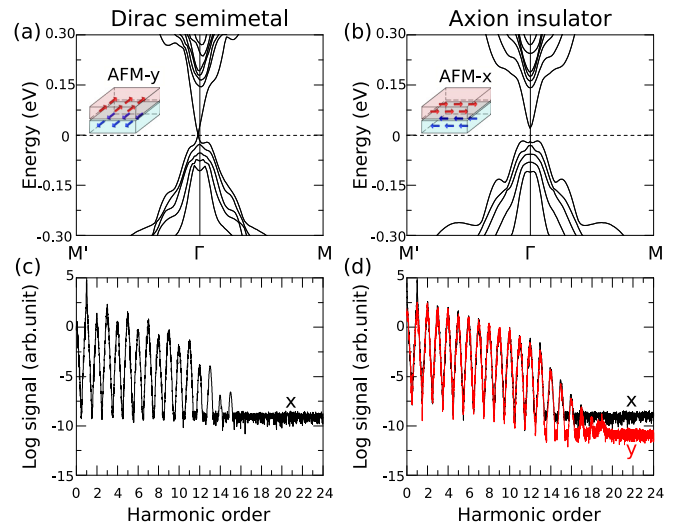


FIG. 3. (a) Electronic structure of the rhombohedral 6-SL  $\text{MnBi}_2\text{Te}_4$  along the high-symmetry lines  $M'-\Gamma-M$  with SOC. The magnetic moments appear antiferromagnetically along the  $y$  axis. The Dirac point appears at the crystal momentum  $(-0.015, 0, 0)\pi/a$ , which is protected by  $\sigma_{xz}$ . This leads to a three-dimensional Dirac semimetal. (b) same as (a), but with magnetic moments along the  $x$  axis. The breaking of  $\sigma_{xz}$  gaps out the Dirac point, indicating an axion insulator state. (c) and (d) Harmonic spectra from the (c) Dirac semimetal and (d) axion insulator with laser polarization along the  $x$  axis. The photon energy of the laser field is  $\hbar\omega = 1.0$  eV, with duration  $\tau = 60$  fs and vector potential amplitude  $A_0 = 0.03$  Vfs/Å.

metries. We first focus on the Dirac semimetallic state. When the laser field is linearly polarized along the  $x$  axis, only harmonics whose polarization is parallel to the laser field are generated, where even and odd harmonics coexist, as shown in Fig. 3(c). Due to the presence of  $\mathcal{IT}$ ,  $\mathcal{I}$  is naturally broken, leaving the crystal momentum  $\vec{k}$  and the time  $t$  invariant. This tells us that the effect of  $\mathcal{IT}$  on the polarization  $\vec{P}(t)$  or HHG is like an identity operation  $E$ , protecting both even and the odd harmonics. However, the perpendicular component of harmonics vanishes, which is required by  $\sigma_{xz}$ . Under the  $x$  polarized laser field,  $\sigma_{xz}$ ,  $E$ , and  $\mathcal{IT}$  belong to the same subgroup [22,46]. The opposite effects of  $\sigma_{xz}$  and  $E/\mathcal{IT}$  on the  $y$  component cancels the corresponding harmonic signals.

Compared to the case of the Dirac semimetallic state, an additional perpendicular component of harmonics is induced in the axion insulator state, as shown in Fig. 3(d). The underlying physics stems from the breaking of  $\sigma_{xz}$  and the remaining of  $E$  and  $\mathcal{IT}$ . Thus, the Dirac semimetallic and axion insulator states present sensitive HHG dependence on  $\sigma_{xz}$ , which can in principle be distinguished from the selectively emerged harmonic component. When the laser field is linearly polarized along the  $y$  axis, distinct harmonics are also observed (see Supplemental Material in more detail).

The change in magnetic orientation has a marked impact on electronic and topological properties. Here, we consider two FM models: FM- $y$  and FM- $x$ . Their band structures are quite different [see Figs. 4(a) and 4(b)], especially for the band crossings near the Fermi energy level, implying the strong influence of magnetic orientation on topological properties. Importantly,  $\sigma_{xz}$  and  $R_y$  are preserved for FM- $y$ , while they



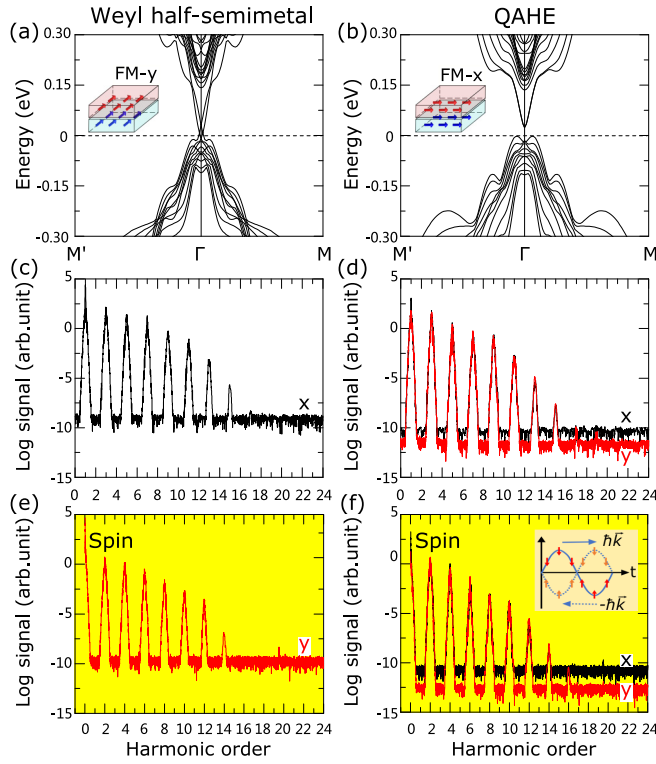


FIG. 4. (a) Electronic structure of 6-SL  $\text{MnBi}_2\text{Te}_4$  along the high-symmetry line  $M'-\Gamma-M$  with SOC. The magnetic moments appear ferromagnetically along the  $y$  axis. Besides  $\mathcal{I}$  and  $E$ , two crystalline symmetries  $\sigma_{xz}$  and  $R_y$  are kept, dictating a Weyl half-semimetallic state. (b) same as (a), but with magnetic moments are along the  $x$  axis. Hence,  $\sigma_{xz}$  and  $R_y$  are broken, leading to QAHE. (c) and (d) Harmonic spectra from the (c) Weyl half-semimetallic state and (d) QAHE with laser polarization along the  $x$  axis. (e) and (f) Spin HHGs for the (e) Weyl half-semimetallic state and (f) QAHE. Inset: solid and dashed lines represent the plane waves differing by a half period. The opposite oscillations mean the opposite propagation directions with  $\hbar\vec{k}$  and  $-\hbar\vec{k}$ , respectively. The parameters of the laser field are the same as those in Fig. 3.

are broken for FM- $x$ . The existence of  $\sigma_{xz}$  dictates a pair of two-fold band crossings near  $\Gamma$  along the high-symmetry lines  $M'-\Gamma-M$  under  $\mathcal{I}$  (see Supplemental Material [31] for more detail), as shown in Fig. 4(a). Meanwhile,  $\sigma_{xz}$  requires a vanishing in-plane Hall conductance [55]. This means the FM- $y$  system is a Weyl half-semimetallic state with Chern number  $C = 0$  [56]. Remarkably, accompanying the magnetic orientation change from FM- $y$  to FM- $x$ , a topological quantum phase transition from  $C = 0$  to  $C = 1$  occurs, which is realized by opening the band gap under band inversion, as shown in Fig. 4(b). This leads to QAHE, which provides quantized edge states for lossless charge-transport applications [5,54,57].

Next, we focus on HHG of FM- $y$ . When the laser field is linearly polarized along the  $x$  axis, only harmonics parallel to the laser field appear, as shown in Fig. 4(c). The perpendicular component disappears. The underlying physics is similar with that of AFM- $y$ . According to our previous work [22], the four symmetries here should be classified into two subgroups:  $E$  and  $\sigma_{xz}$  form one subgroup, while  $\mathcal{I}$  and  $R_y$  constitute another one. The two subgroups have exactly opposite  $y$  com-

ponent values. As a result, they cancel out the corresponding harmonic signals. Compared to the AFM configuration, we observe that, due to the appearance of  $\mathcal{I}$ , even signals are removed from HHG. In the case of FM- $x$ , the perpendicular component appears again, protected by  $\sigma_{xz}$  and  $R_y$ , as shown in Fig. 4(c). Based on the above results, we can see that the four topological phases generate four distinct high harmonics. This serves as the basis of HHG as a potential tool to detect the topological quantum states.

Unlike AFM and our previous work [22,46], there exist nonzero net magnetic moments for FM, which results from the  $\mathcal{IT}$  breaking. Analogous to the induced polarization of the system, the laser field can make the spin change through  $\vec{S}(t) = \sum_{\mathbf{k}} \text{Tr}[\rho_{\mathbf{k}}(t)\hat{S}_{\mathbf{k}}]$ , with  $\hat{S}_{\mathbf{k}}$  being the spin operator. This change would also generate high harmonics as it shares the same dynamical density matrix as  $\vec{P}(t)$ . For differentiating it from the HHG of  $\vec{P}(t)$  (henceforward denoted as optical HHG), we denote it as spin HHG. When the laser field is linearly polarized along the  $x$  axis, the perpendicular component of spin HHG appears for FM- $y$  [see Fig. 4(e)], which is contrary to the optical HHG [see Fig. 4(c)]. The underlying physics comes from the different operations of symmetries on the spin in comparison with the space coordinate, which is directly related to the improper rotation of the point group. Here the improper rotations include  $\mathcal{I}$  and  $\sigma_{xz}$ , while the proper rotations contain  $E$  and  $R_y$ . For  $\mathcal{I}$ , it makes the transformation of space coordinate  $\vec{r}$  inverse and leaves the spin  $\vec{S}$  unchanged. Thus, it is unified with  $E$  to form a subgroup, protecting the spin invariant. For the symmetry  $\sigma_{xz}$ , it changes the space coordinate from  $(x, y, z)$  to  $(x, -y, z)$  and the spin from  $(S_x, S_y, S_z)$  to  $(-S_x, S_y, -S_z)$ . In this context, it should be combined with  $R_y$  to form another subgroup, reflecting the spin along the  $y$  axis. Under the operation of the two subgroups, the spin harmonics cancel along the  $x$  and  $z$  axes, but remain along the  $y$  axis.

In the case of FM- $x$ ,  $\sigma_{xz}$  and  $R_y$  are broken, whereas  $E$  and  $\mathcal{I}$  still hold. Based on the above analysis, both  $E$  and  $\mathcal{I}$  preserve the spin. Thus, both the parallel and perpendicular components appear in the spin HHG, as shown in Fig. 4(f).

It is also noticed that only even harmonics appear in the spin HHG. This is quite different from the optical HHG [58,59]. Here, we adopt the symmetries  $E$  and  $\mathcal{I}$  for FM- $x$  to unveil this mystery. Although  $E$  and  $\mathcal{I}$  have no effect on the spin, they can affect the spin change  $\vec{S}(t)$  or the spin HHG through the laser field. As an element of the two symmetries,  $\mathcal{I}$  dictates the system invariant under the change  $\vec{r} \rightarrow -\vec{r}$ . We take a plane wave  $\Psi(t) = e^{i(\vec{k}\cdot\vec{r}-\omega t)}$  to demonstrate the operation of  $\mathcal{I}$ .  $\mathcal{I}$  gives us  $\Psi'(t) = \mathcal{I}\Psi(t) = e^{-i(\vec{k}\cdot\vec{r}-i\omega t)}$ . This means that  $\mathcal{I}$  requires  $\Psi'(t)$  with wave vector  $-\hbar\vec{k}$  to move in the opposite direction. Since the spin does not change, the symmetries only impinge on the laser field, which is indirectly through the interaction Hamiltonian as

$$\mathcal{H}_I(t) = \frac{e}{m_e} \hat{P} \cdot \vec{A}(\vec{r}, t) + \frac{e}{m_e} \hat{S} \cdot \nabla \times \vec{A}(\vec{r}, t) + \frac{e^2}{2m_e} [\vec{A}(\vec{r}, t)]^2. \quad (3)$$

The vector potential of laser field has the form  $\vec{A}(\vec{r}, t) = [\mathcal{A}_0 e^{i(\vec{k}\cdot\vec{r}-\omega t)} + \mathcal{A}_0^* e^{-i(\vec{k}\cdot\vec{r}-\omega t)}] e^{\tau^2/t^2} \hat{e}_r$ , where  $\mathcal{A}_0$  is the complex

amplitude and  $\tau$  the duration of laser pulse. The first two terms of the right-hand side of Eq. (3) depend linearly on  $\vec{A}(\vec{r}, t)$ , and the third one depends on it quadratically. In our realistic calculations, we ignore the last two terms, each being much smaller than the first one. Equation (3) tells us that the laser field enters the dynamic density matrix  $\rho$  based on the time-dependent Liouville equation, and subsequently affects the spin HHG. In the time domain, the opposite motion of the plane wave is equivalent to adding an additional half period to the laser field. In other words,  $E$  and  $\mathcal{I}$  enforce a time constraint of  $t \rightarrow t + T/2$  to the laser field [60], realizing the laser field invariant with an opposite oscillation [see the inset of Fig. 4(f)]. As a result, only even harmonics are allowed in the spin HHG [46]. This finding also holds for  $\sigma_{xz}$  and  $R_y$ , where their  $y$  components have the same effect as  $E$  and  $\mathcal{I}$ .

Finally, we consider HHG generated from the magnetic moments along the  $z$  axis. Here, both  $\sigma_{xz}$  and  $R_y$  are broken generally, whereas  $C_3$  holds. Similarly, distinct harmonic spectra can be obtained under the circularly polarized laser field (see Supplemental Material [31] for more details).

In experimental respect, our obtained HHG is up to  $\sim 15$ th order, where the 6-SL  $\text{MnBi}_2\text{Te}_4$  with thickness of about 9 nm is taken and the laser intensity is about  $0.28 \times 10^{11}$  W/cm<sup>2</sup>. Under similar laser intensities, monolayer  $\text{MoS}_2$  and graphene generate HHG up to the 13th and 9th orders, respectively [61,62]. In addition, if we compare  $\text{MnBi}_2\text{Te}_4$  with monolayer Fe [18], the signal from  $\text{MnBi}_2\text{Te}_4$  would be much stronger. This is because the signal of HHG is proportional to the thickness of the sample [61]. Thus, HHG predicted in

this work would be easily obtained in experiment if the proper thickness of  $\text{MnBi}_2\text{Te}_4$  is utilized.

#### IV. SUMMARY AND CONCLUSIONS

In this work, we have demonstrated that rhombohedral  $\text{MnBi}_2\text{Te}_4$  film has four magnetic configuration-mediated topological phases, generating four distinctive high-harmonic spectra. Dirac semimetal and an axion insulator in  $\mathcal{IT}$  invariant antiferromagnets dictate the high harmonics, including both even and odd orders. By contrast, the Weyl half semimetal and QAHE from the broken  $\mathcal{IT}$  ferromagnets give rise to only odd high harmonics. In addition, certain crystalline symmetries selectively generate the parallel and/or perpendicular components of harmonics, which are directly correlated to the physical origin of topological quantum states. Our results reveal that HHG has the capacity of detecting the topological phases mediated by magnetic configurations and provide a theoretical guide for experimental researchers. Although the Berry curvature is important at the topological classification of the novel materials, it is hard to extract the contribution of Berry curvature solely to HHG at present stage. This would be the focus of future research.

#### ACKNOWLEDGMENTS

This work was supported by the National Science Foundation of China under Grant Nos. 11874189 and 11774139. We also acknowledge the Fermi cluster at Lanzhou University for providing computational resources. G.P.Z. was supported by the U.S. Department of Energy under Contract No. DE-FG02-06ER46304.

- 
- [1] X.-L. Qi and S.-C. Zhang, *Rev. Mod. Phys.* **83**, 1057 (2011).
  - [2] M. Z. Hasan and C. L. Kane, *Rev. Mod. Phys.* **82**, 3045 (2010).
  - [3] P. Tang, Q. Zhou, G. Xu, and S.-C. Zhang, *Nat. Phys.* **12**, 1100 (2016).
  - [4] C.-Z. Chang, J. Zhang, X. Feng, J. Shen, Z. Zhang, M. Guo, K. Li, Y. Ou, P. Wei, L.-L. Wang, Z.-Q. Ji, Y. Feng, S. Ji, X. Chen, J. Jia, X. Dai, Z. Fang, S.-C. Zhang, K. He, Y. Wang, L. Lu, X.-C. Ma, and Q.-K. Xue, *Science* **340**, 167 (2013).
  - [5] R. Yu, W. Zhang, H.-J. Zhang, S.-C. Zhang, X. Dai, and Z. Fang, *Science* **329**, 61 (2010).
  - [6] R. Li, J. Wang, X. L. Qi, and S.-C. Zhang, *Nat. Phys.* **6**, 284 (2010).
  - [7] E. Majorana, *Nuovo Cim.* **14**, 171 (1937).
  - [8] B.-J. Yang and N. Nagaosa, *Nat. Commun.* **5**, 4898 (2014).
  - [9] Y. Tokura and N. Nagaosa, *Nat. Commun.* **9**, 3740 (2018).
  - [10] Y. Sanari, T. Otobe, Y. Kanemitsu, and H. Hirori, *Nat. Commun.* **11**, 3069 (2020).
  - [11] T. T. Luu and H. J. Wörner, *Nat. Commun.* **9**, 916 (2018).
  - [12] G. McCaul, C. Orthodoxou, K. Jacobs, G. H. Booth, and D. I. Bondar, *Phys. Rev. Lett.* **124**, 183201 (2020).
  - [13] B. Keimer and J. E. Moore, *Nat. Phys.* **13**, 1045 (2017).
  - [14] P. B. Corkum and F. Krausz, *Nat. Phys.* **3**, 381 (2007).
  - [15] M. Wu, S. Ghimire, D. A. Reis, K. J. Schafer, and M. B. Gaarde, *Phys. Rev. A* **91**, 043839 (2015).
  - [16] Y. S. You, D. A. Reis, and S. Ghimire, *Nat. Phys.* **13**, 345 (2017).
  - [17] F. Langer, M. Hohenleutner, U. Huttner, S. W. Koch, M. Kira, and R. Huber, *Nat. Photon.* **11**, 227 (2017).
  - [18] G. P. Zhang, M. S. Si, M. Murakami, Y. H. Bai, and T. F. George, *Nat. Commun.* **9**, 3031 (2018).
  - [19] A. Chacón, D. Kim, W. Zhu, S. P. Kelly, A. Dauphin, E. Pisanty, A. S. Maxwell, A. Picón, M. F. Ciappina, D. E. Kim, C. Ticknor, A. Saxena, and M. Lewenstein, *Phys. Rev. B* **102**, 134115 (2020).
  - [20] W. P. Su, J. R. Schrieffer, and A. J. Heeger, *Phys. Rev. Lett.* **42**, 1698 (1979).
  - [21] D. Bauer and K. K. Hansen, *Phys. Rev. Lett.* **120**, 177401 (2018).
  - [22] L. Jia, Z. Zhang, D. Z. Yang, M. S. Si, G. P. Zhang, and Y. S. Liu, *Phys. Rev. B* **100**, 125144 (2019).
  - [23] P. Hohenber and W. Kohn, *Phys. Rev.* **136**, B864 (1964).
  - [24] J. P. Perdew and Y. Wang, *Phys. Rev. B* **45**, 13244 (1992).
  - [25] M. Hohenleutner, F. Langer, O. Schubert, M. Knorr, U. Huttner, S. W. Koch, M. Kira, and R. Huber, *Nature* **523**, 572 (2015).
  - [26] G. Ndabashimiye, S. Ghimire, M. Wu, D. A. Browne, K. J. Schafer, M. B. Gaarde, and D. A. Reis, *Nature* **534**, 520 (2016).
  - [27] S. Yu. Kruchinin, F. Krausz, and V. S. Yakovlev, *Rev. Mod. Phys.* **90**, 021002 (2018).

- [28] H. Lakhotia, H. Y. Kim, M. Zhan, S. Hu, S. Meng, and E. Goulielmakis, *Nature* **583**, 55 (2020).
- [29] M. A. Sentef, *Nature* **583**, 35 (2020).
- [30] G. P. Zhang, Y. H. Bai, and T. F. George, *Phys. Rev. B* **80**, 214415 (2009).
- [31] See Supplemental Material at <http://link.aps.org/supplemental/10.1103/PhysRevB.102.174314> for more detailed discussions and results of HHG on other magnetic configurations, which also includes Refs. [63–67].
- [32] D. S. Lee, T.-H. Kim, C.-H. Park, C.-Y. Chung, Y. S. Lim, W.-S. Seo, and H.-H. Park, *Cryst. Eng. Comm.* **15**, 5532 (2013).
- [33] Y.-J. Hao, P. Liu, Y. Feng, X.-M. Ma, E. F. Schwier, M. Arita, S. Kumar, C. Hu, R. Lu, M. Zeng, Y. Wang, Z. Hao, H.-Y. Sun, K. Zhang, J. Mei, N. Ni, L. Wu, K. Shimada, C. Chen, Q. Liu, and C. Liu, *Physical Review X* **9**, 041038 (2019).
- [34] P. Swatek, Y. Wu, L.-L. Wang, K. Lee, B. Schrunk, J. Yan, and A. Kaminski, *Phys. Rev. B* **101**, 161109(R) (2020).
- [35] J. Zhang and Z. Liu, and J. Wang, *Phys. Rev. B* **100**, 165117 (2019).
- [36] J. Li, Y. Li, S. Du, Z. Wang, B.-L. Gu, S.-C. Zhang, K. He, W. Duan, and Y. Xu, *Sci. Adv.* **5**, eaaw5685 (2019).
- [37] J. Li, C. Wang, Z. Zhang, B.-L. Gu, W. Duan, and Y. Xu, *Phys. Rev. B* **100**, 121103 (2019).
- [38] C. Liu, Y. Wang, H. Li, Y. Wu, Y. Li, J. Li, K. He, Y. Xu, J. Zhang, and Y. Wang, *Nat. Mater.* **19**, 522 (2020).
- [39] D. Zhang, M. Shi, T. Zhu, D. Xing, and H. Zhang, and J. Wang, *Phys. Rev. Lett.* **122**, 206401 (2019).
- [40] M. M. Otrokov, I. P. Rusinov, M. Blanco-Rey, M. Hoffmann, A. Y. Vyazovskaya, S. V. Eremeev, A. Ernst, P. M. Echenique, A. Arnau, and E. V. Chulkov, *Phys. Rev. Lett.* **122**, 107202 (2019).
- [41] M. M. Otrokov, I. I. Klimovskikh, H. Bentmann, D. Estyunin, A. Zeugner, Z. S. Aliev, S. Gaß, A. U. B. Wolter, A. V. Koroleva, A. M. Shikin, M. Blanco-Rey, M. Hoffmann, I. P. Rusinov, A. Yu. Vyazovskaya, S. V. Eremeev, Yu. M. Koroteev, V. M. Kuznetsov, F. Freyse, J. Sánchez-Barriga, I. R. Amiraslanov, M. B. Babanly, N. T. Mamedov, N. A. Abdullayev, V. N. Zverev, A. Alfonsov, V. Kataev, B. Büchner, E. F. Schwier, S. Kumar, A. Kimura, L. Petaccia, G. Di Santo, R. C. Vidal, S. Schatz, K. Kißner, M. Ünzelmann, C. H. Min, Simon Moser, T. R. F. Peixoto, F. Reinert, A. Ernst, P. M. Echenique, A. Isaeva, and E. V. Chulkov, *Nature* **576**, 416 (2019).
- [42] R.-X. Zhang, F. Wu, and S. Das Sarma, *Phys. Rev. Lett.* **124**, 136407 (2020).
- [43] C. Chen, Z. Song, J.-Z. Zhao, Z. Chen, Z.-M. Yu, X.-L. Sheng, and S. A. Yang, *Phys. Rev. Lett.* **125**, 056402 (2020).
- [44] Y. Gong, J. Guo, J. Li, K. Zhu, M. Liao, X. Liu, Q. Zhang, L. Gu, L. Tang, X. Feng, D. Zhang, W. Li, C. Song, L. Wang, P. Yu, X. Chen, Y. Wang, H. Yao, W. Duan, Y. Xu, S.-C. Zhang, X. Ma, Q.-K. Xue, and K. He, *Chin. Phys. Lett.* **36**, 076801 (2019).
- [45] J. Cui, M. Shi, H. Wang, F. Yu, T. Wu, X. Luo, J. Ying, and X. Chen, *Phys. Rev. B* **99**, 155125 (2019).
- [46] L. Jia, Z. Zhang, D. Z. Yang, Y. Q. Liu, M. S. Si, G. P. Zhang, and Y. S. Liu, *Phys. Rev. B* **101**, 144304 (2020).
- [47] Y. Tokura, K. Yasuda, and A. Tsukazaki, *Nat. Rev. Phys.* **1**, 126 (2019).
- [48] W. Feng, J.-P. Hanke, X. Zhou, G.-Y. Guo, S. Blügel, Y. Mokrousov, and Y. Yao, *Nat. Commun.* **11**, 118 (2020).
- [49] B. Lv, T. Qian, and H. Ding, *Nat. Rev. Phys.* **1**, 609 (2019).
- [50] J. Hu, Y. L. Zhu, D. Graf, Z. J. Tang, J. Y. Liu, and Z. Q. Mao, *Phys. Rev. B* **95**, 205134 (2017).
- [51] B. M. Wojek, M. H. Berntsen, V. Jonsson, A. Szczerbakow, P. Dziawa, B. J. Kowalski, T. Story, and O. Tjernberg, *Nat. Commun.* **6**, 8463 (2015).
- [52] C.-Z. Chang, W. Zhao, D. Y. Kim, H. Zhang, B. A. Assaf, D. Heiman, S.-C. Zhang, C. Liu, M. H. W. Chan, and J. S. Moodera, *Nat. Mater.* **14**, 473 (2015).
- [53] S. Wiedmann, A. Jost, B. Fauqué, J. van Dijk, M. J. Meijer, T. Khouri, S. Pezzini, S. Grauer, S. Schreyeck, C. Brüne, H. Buhmann, L. W. Molenkamp, and N. E. Hussey, *Phys. Rev. B* **94**, 081302 (2016).
- [54] E. D. L. Rienks, S. Wimmer, J. Sánchez-Barriga, O. Caha, P. S. Mandal, J. Ruzicka, A. Ney, H. Steiner, V. V. Volobuev, H. Groiss, M. Albu, G. Kothleitner, J. Michalicka, S. A. Khan, J. Minar, H. Ebert, G. Bauer, F. Freyse, A. Varyhalov, O. Rader, and G. Spingholz, *Nature* **576**, 423 (2019).
- [55] X. Liu, H.-C. Hsu, and C.-X. Liu, *Phys. Rev. Lett.* **111**, 086802 (2013).
- [56] J.-Y. You, C. Chen, Z. Zhang, X.-L. Sheng, S. A. Yang, and G. Su, *Phys. Rev. B* **100**, 064408 (2019).
- [57] M. Onoda and N. Nagaosa, *Phys. Rev. Lett.* **90**, 206601 (2003).
- [58] Z. Sun, Y. Yi, T. Song, G. Clark, B. Huang, Y. Shan, S. Wu, D. Huang, C. Gao, Z. Chen, M. McGuire, T. Cao, D. Xiao, W.-T. Liu, W. Yao, X. Xu, and S. Wu, *Nature* **572**, 497 (2019).
- [59] R. Fei, W. Song, and L. Yang, *Phys. Rev. B* **102**, 035440 (2020).
- [60] O. E. Alon, V. Averbukh, and N. Moiseyev, *Phys. Rev. Lett.* **80**, 3743 (1998).
- [61] H. Liu, Y. Li, Y. S. You, S. Ghimire, T. F. Heinz, and D. A. Reis, *Nat. Phys.* **13**, 262 (2017).
- [62] N. Yoshikawa, T. Tamaya, and K. Tanaka, *Science* **356**, 736 (2017).
- [63] P. Blaha, K. Schwarz, P. Sorantin, and S. B. Trickey, *Comput. Phys. Commun.* **59**, 399 (1990).
- [64] J. P. Perdew, K. Burke, and M. Ernzerhof, *Phys. Rev. Lett.* **77**, 3865 (1996).
- [65] P. Blaha, K. Schwarz, G. K. H. Madsen, D. Kvasnicka, and J. Luitz, WIEN2k, *An Augmented Plane Wave + Local Orbitals Program for Calculating Crystal Properties* (Techn. Universität Wien, Wien, Austria, 2001).
- [66] A. A. Mostofi, J. R. Yates, Y.-S. Lee, I. Souza, D. Vanderbilt, and N. Marzari, *Comput. Phys. Commun.* **178**, 685 (2008).
- [67] von Neumann and J. Wigner, *Z. Phys.* **30**, 467 (1929).